International Journal of Solids and Structures 230–231 (2021) 111164

Contents lists available at ScienceDirect

International Journal of Solids and Structures

journal homepage: www.elsevier.com/locate/ijsolstr

A numerical study on elastic properties of low-density two-dimensional networks of crosslinked long fibers

Soham Mane [a], Fardin Khabaz [b], Roger T. Bonnecaze [c], Kenneth M. Liechti [a], Rui Huang [a,*]

[a] Department of Aerospace Engineering and Engineering Mechanics, University of Texas, Austin, TX 78712, United States
[b] Department of Chemical, Biomolecular, and Corrosion Engineering, School of Polymer Science and Polymer Engineering, University of Akron, Akron, OH 44325, United States
[c] Department of Chemical Engineering, University of Texas, Austin, TX 78712, United States

ARTICLE INFO

Article history:
Received 30 March 2021
Received in revised form 6 July 2021
Accepted 8 July 2021
Available online 14 July 2021

Keywords:
Elastic properties
Periodic networks
Random networks
Buckling

ABSTRACT

Fiber-based materials are prevalent in nature and in engineering applications. Microscopically, these materials resemble a discrete assembly of crosslinked or entangled fibers. To understand the relationship between the effective mechanical properties and the underlying microstructures, we consider a variety of periodic and random two-dimensional (2D) networks of crosslinked long fibers. The linearly elastic properties of periodic 2D networks (e.g., square, triangular and Kagome) are well understood. However, for low-density networks, cooperative buckling of the fiber segments can take place at small strains, leading to nonlinear, anisotropic elastic behaviors. A transition from stretch to bending and then back to stretch dominated deformation is predicted for the Kagome and triangular networks. For random 2D networks, the elastic behaviors are different. Under uniaxial tension, the stress–strain behavior is statistically isotropic and slightly nonlinear, dominated by stretch of the fibers aligned closely to the loading direction. Meanwhile, stochastic buckling occurs continuously in the random networks, leading to significant lateral contraction. Consequently, while the effective Young's modulus follows a nearly linear scaling with respect to the relative density, the effective Poisson's ratio exhibits a transition from stretch to bending dominated mode as the relative density decreases. A statistical analysis is performed to estimate the relative errors of the effective properties that depend on both the computational box size and the number of random realizations. The comparison between the periodic and random 2D networks highlights the profound effects of the network topology on the effective elastic properties.

1. Introduction

Fiber-based materials are prevalent both in nature and in engineering applications. As an example, fibrous extracellular matrices (ECM) consist of three-dimensional (3D) collagen networks with long-range force transmission and peculiar mechanical properties enabling a variety of cell interactions (Abhilash et al., 2014; Wang et al., 2014; Hall et al., 2016; Ban et al., 2018; Ban et al., 2019). Paper is another example made from natural materials and has long been considered as a random fiber network with anisotropic elastic properties due to process-dependent fiber orientations (Cox, 1952; Ostoja-Starzewski and Stahl, 2000). A recent development of nanopaper made of nano-fibrillated cellulose networks with fiber diameters down to 11 nm has demonstrated excellent mechanical properties in both strength and toughness (Zhu et al., 2015; Meng and Wang, 2019). Carbon nanotubes (CNTs), nanofibers and nanowires have also been used to make network materials such as fabrics (Smith et al., 2010; Holmberg et al., 2012) and aerogels (Jung et al., 2012; Jung et al., 2014; Wu et al., 2018; Yu et al., 2019). Besides random fiber networks, periodic network structures have recently emerged as lattice or cellular materials that may be hierarchically architected to achieve lightweight, flaw-tolerant, and ultrastrong properties (Fleck et al., 2010; Meza et al., 2014; Meza et al, 2015; Schwaiger et al., 2019; Xia et al., 2019; Zhang et al., 2019).

To understand the relationship between the effective mechanical properties and the underlying microstructures for the random or periodic fiber networks, both 2D and 3D network models have been developed (Fleck et al., 2010; Picu, 2011; Broedersz and MacKintosh, 2014; Merson and Picu, 2020). The linearly elastic properties under infinitesimal strain have been predicted analytically for a variety of periodic networks (Christensen, 2000; Ostoja-Starzewski, 2002; Romijn and Fleck, 2007). For the random fiber networks, different scaling relations have been found

* Corresponding author.
E-mail address: ruihuang@mail.utexas.edu (R. Huang).

https://doi.org/10.1016/j.ijsolstr.2021.111164
0020-7683/

between the effective elastic moduli and network parameters (Cox, 1952; Wu and Dzenis, 2005; Broedersz et al., 2012; Shahsavari and Picu, 2012; Shahsavari and Picu, 2013; Ban et al., 2016), depending on the network topology. In particular, a transition from stretch dominated (affine) deformation to bending dominated (non-affine) deformation has been predicted for random networks as the relative density decreases. Beyond small-strain linear elasticity, it has been found that the random fiber networks typically stiffen at large strains (Onck et al., 2005; Huisman et al., 2007; Broedersz et al., 2008; Islam and Picu, 2018). Moreover, inelastic mechanical properties such as strength and toughness have also been simulated in some network models (Romijn and Fleck, 2007; Åström et al., 2008; Koh and Oyen, 2012; Kulachenko and Uesaka, 2012; Sozumert et al., 2020). In this study, we focus on the linear and nonlinear elastic properties of low-density 2D networks of crosslinked long fibers. As illustrated in Fig. 1, the long fibers may form a variety of periodic lattices, each with a characteristic length for the unit cell. Alternatively, for a random network of long fibers (Fig. 1d), statistically representative elements may be used to simulate the effective mechanical properties. Unlike most of the previous works on random fiber networks, we assume that the fiber lengths are greater than the size of the statistically representative element so that fibers have no dangling ends within the element. This assumption eliminates the fiber length as one of the network parameters so that the fiber segment length(s) and diameter become the most relevant, which is also the case for the periodic networks in Fig. 1 (a–c). As a result, the effective elastic properties of these 2D networks depend primarily on the relative density and the network topology. In the remainder of this paper, we first present analytical and numerical results for the periodic 2D networks (Section 2), comparing the square, triangular and Kagome networks in both the linear and nonlinear regimes. Then, random 2D networks are considered in Section 3 including a statistical analysis of the network parameters and elastic properties. A comparison between the periodic and random 2D networks illustrates the profound effects of network topology (random versus periodic) on the elastic properties, as summarized in Section 4.

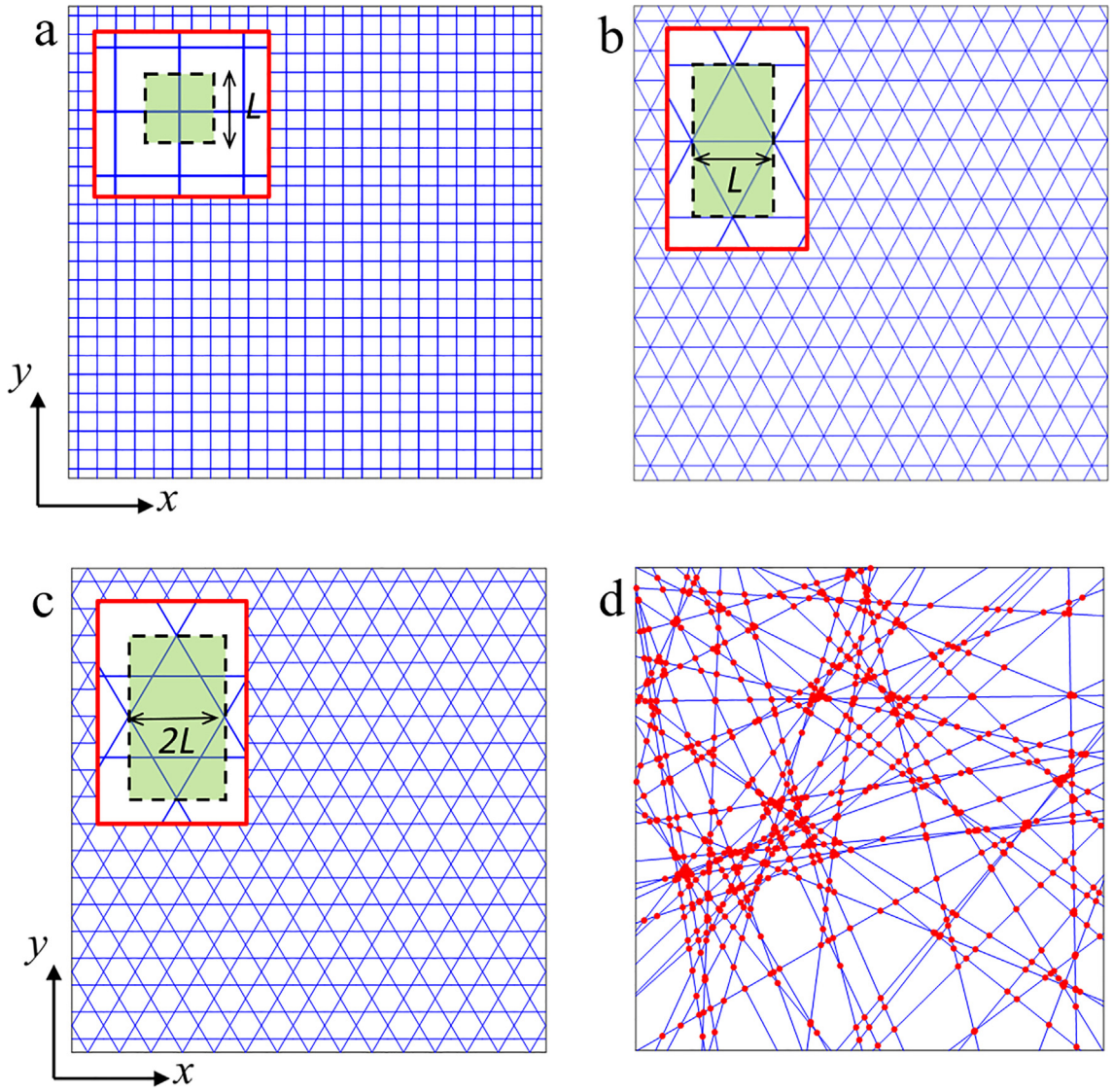

Fig. 1. Periodic and random 2D networks: (a) square network; (b) triangular network; (c) Kagome network; (d) random network (with all joints marked as red dots). Insets show unit cells for the periodic networks with a segment length *L*. (For interpretation of the references to color in this figure legend, the reader is referred to the web version of this article.)

2. Periodic 2D networks

2.1. Linearly elastic properties

A periodic 2D network has two relevant length scales: the fiber diameter d and the segment length L, as illustrated in Fig. 1 (a-c). The relative density of the periodic 2D network can be written as:

$$\rho = \frac{Ad}{L} \tag{1}$$

where A is a constant depending on the network topology and the cross section of the fibers. Table 1 lists the values of A for periodic networks consisting of fibers with a circular cross section, which are different from those for a rectangular cross section in Romijn and Fleck (2007).

Assuming linear elasticity for the fiber material and rigid (welded) joints between the fibers, the effective in-plane elastic moduli of the periodic 2D networks depend on the relative density and can be predicted as (Romijn and Fleck, 2007):

$$E_{eff} = B\rho^b E_f \tag{2}$$

$$G_{eff} = C\rho^c E_f \tag{3}$$

where E_{eff} is the effective Young's modulus and G_{eff} is the effective shear modulus, both proportional to E_f, Young's modulus of the fiber material; B, C, b and c are constants depending on the network topology (see Table 1). In addition, the effective in-plane Poisson's ratio (υ_{12}) is independent of the relative density but depends on the network topology as listed in Table 1.

According to Table 1, the square network is highly anisotropic with different scaling for the effective Young's modulus (b = 1) and shear modulus (c = 3), while the triangular and Kagome networks are isotropic (b = c = 1) with a Poisson's ratio of 1/3. Evidently, the cubic scaling (c = 3) for the effective shear modulus of the square network indicates the bending dominated deformation of the fibers under shear, whereas the linear scaling for the effective Young's modulus (b = 1) indicates the stretch dominated fiber deformation under uniaxial stresses; the linear scaling for both moduli of the triangular and Kagome networks indicates stretch dominated fiber deformation in both loading modes. It should be noted that the analytical predictions are applicable only under infinitesimal strains. Notably, for the triangular and Kagome networks, the linear scaling of the effective moduli persists at low density ($\rho \ll 1$), with no transition to the bending dominated behavior as predicted for the random networks (Wu and Dzenis, 2005; Broedersz et al., 2012; Shahsavari and Picu, 2012; Ban et al., 2016).

For the triangular and Kagome networks (Fig. 1, b and c), the effective in-plane stress–strain relation in the linear regime can be written in a matrix form as:

$$\begin{pmatrix} \sigma_{11} \\ \sigma_{22} \\ \sigma_{12} \end{pmatrix} = \begin{bmatrix} C_{11} & C_{12} & 0 \\ C_{21} & C_{22} & 0 \\ 0 & 0 & C_{33} \end{bmatrix} \begin{pmatrix} \varepsilon_{11} \\ \varepsilon_{22} \\ \varepsilon_{12} \end{pmatrix} \tag{4}$$

Table 1
Parameters for the effective properties of periodic 2D networks.

	Square	Triangular	Kagome
A	$\pi/2$	$\sqrt{3}\pi/2$	$\sqrt{3}\pi/4$
B	1/2	1/3	1/3
b	1	1	1
C	$3/(32\pi^2)$	1/8	1/8
c	3	1	1
ν_{12}	0	1/3	1/3

where $C_{11} = C_{22} = \frac{9}{8}E_{eff}$, $C_{33} = 2G_{eff}$, and $C_{12} = C_{21} = \frac{3}{8}E_{eff}$. It can be shown that the effective Young's modulus and Poisson's ratio of a triangular/Kagome network are independent of the loading direction under uniaxial stresses.

For a square network (Fig. 1a), we have: $C_{11} = C_{22} = E_{eff}$, $C_{33} = 2G_{eff}$, and $C_{12} = C_{21} = 0$ in Eq. (4). Thus, the effective 2D stiffness of a square network is anisotropic with the symmetry of a square lattice (orthotropic). In this case, the effective Young's modulus and Poisson's ratio depend on the loading direction under uniaxial stress. By considering a square network subject to uniaxial stress in an arbitrary direction θ (the angle between the loading direction and the fibers; Fig. 2), we obtain the effective Young's modulus as a function of θ as

$$E_\theta = E_{eff}\left[1 + (\eta - 2)\sin^2\theta\cos^2\theta\right]^{-1} \tag{5}$$

where $\eta = \frac{E_{eff}}{G_{eff}} = 8\rho^{-2}$. Interestingly, if $\eta = 2$, the effective Young's modulus becomes isotropic! This however requires an unrealistically high relative density, $\rho = 2$. Typically, with $\rho \ll 1$, we have $\eta \gg 1$ and thus the effective Young's modulus is highly anisotropic (see Fig. 2a). While the maximum effective modulus is E_{eff} for $\theta = 0$ and 90° (parallel to the fibers), the minimum modulus is at $\theta = 45^\circ$, with $E_{min} = 4E_{eff}[2 + \eta]^{-1} \approx 4G_{eff}$, where the approximation is made for $\eta \gg 2$. Therefore, the maximum and minimum Young's moduli have different scaling relations with the relative density: $E_{eff} \sim \rho$ (stretch dominated fiber deformation) and $E_{min} \sim \rho^3$ (bending dominated fiber deformation). A transition from the linear scaling to the cubic scaling for the Young's modulus is thus predicted for the square network as the loading direction changes. With $\rho \ll 1$ for low density square networks, the difference between the minimum and maximum Young's moduli could be several orders of magnitude (Fig. 2a).

Similarly, the effective Poisson's ratio of a square network can be obtained as a function of θ as

$$\nu_\theta = \frac{(\eta - 2)\sin^2 2\theta}{4 + (\eta - 2)\sin^2 2\theta} \tag{6}$$

which is zero for $\theta = 0$ and 90° but is approximately 1 for $\theta = 45^\circ$, for a low-density square network ($\rho \ll 1$) as shown in Fig. 2b. The large Poisson's ratio ($\nu_\theta \approx 1$) again indicates bending dominated fiber deformation.

2.2. Nonlinear elastic properties

Numerical simulations were conducted using the commercial finite element package ABAQUS to simulate the nonlinearly elastic behavior of the periodic 2D networks under uniaxial stresses. The fibers were modeled using the Timoshenko beam elements (B22) with nonlinear geometry for finite strain, and the joints were assumed to be rigid (welded). The fiber material was assumed to be isotropic and linearly elastic in terms of the Cauchy stress and the logarithmic strain, with Young's Modulus E_f and Poisson's ratio ν_f. Periodic boundary conditions were assumed for the unit cells (Fig. 1, a-c), and only the in-plane deformation is considered for the present study. The effective stress for the network was calculated with respect to a rectangular cross section area with a thickness equal to the fiber diameter.

First, for the square networks under uniaxial tension parallel to the fiber directions ($\theta = 0$ and 90°), geometric nonlinearity leads to slightly nonlinear behavior (in terms of the nominal stress and nominal strain) when the axial strain is relatively large (e.g., $\varepsilon > 0.05$), as shown in Fig. 3a. Recall that the fiber material was assumed to be linearly elastic in terms of the Cauchy stress and the logarithmic strain, but nonlinear in terms of the nominal stress

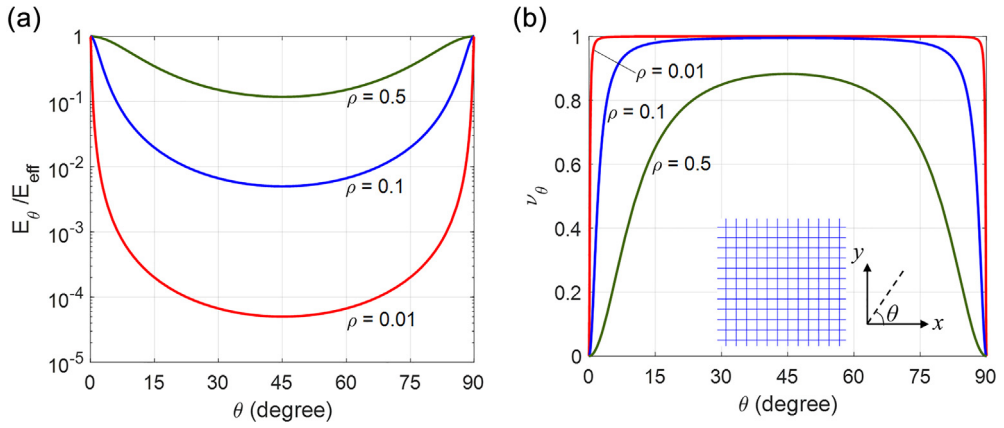

Fig. 2. Effective Young's modulus (a) and Poisson's ratio (b) of square networks (with different relative densities) versus the direction of uniaxial tension.

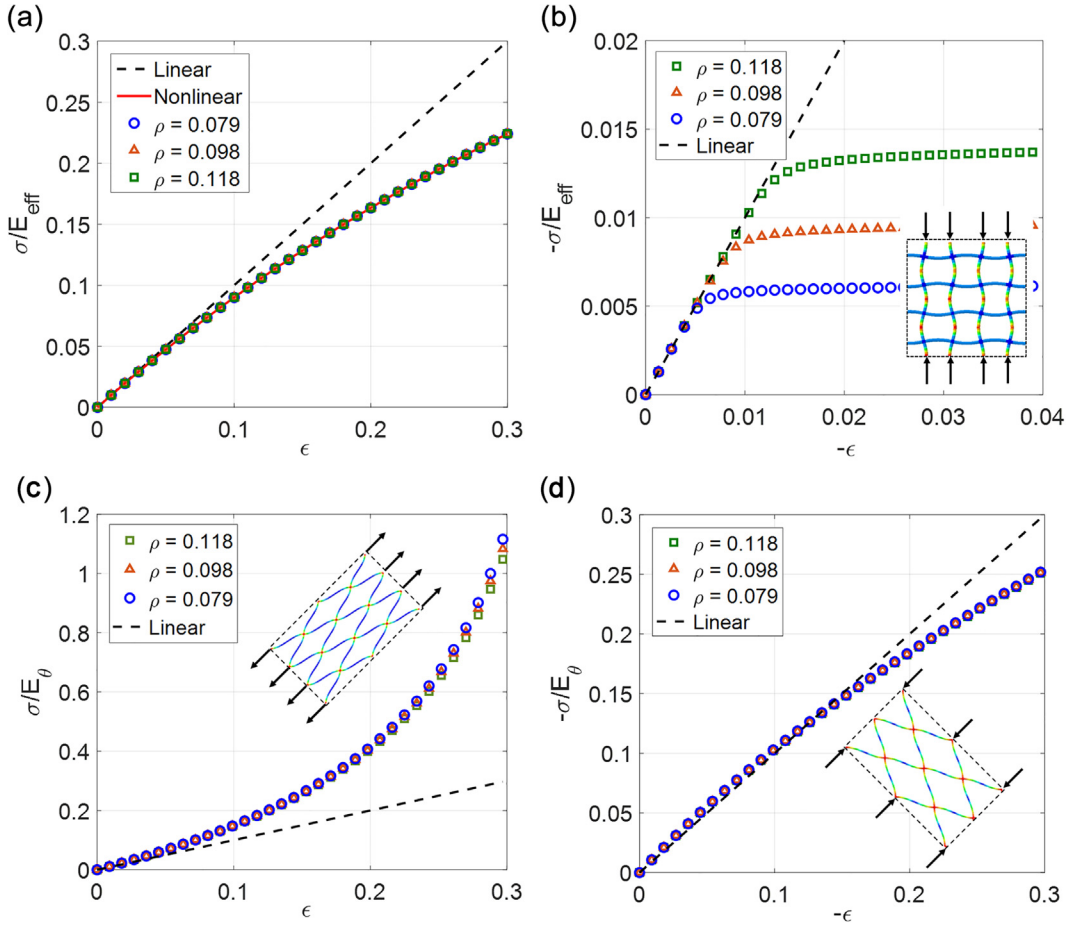

Fig. 3. Nonlinear elastic behavior of square networks: (a) under uniaxial tension ($\theta = 0$ or 90°); (b) under uniaxial compression ($\theta = 90^\circ$); inset shows cooperative buckling of fibers. (c) Under uniaxial tension with $\theta = 45^\circ$, and (d) under uniaxial compression with $\theta = 45^\circ$; insets show deformation of fibers with color contours for the strain energy density distributions.

and nominal strain (shown as the solid line in Fig. 3a). In this case, the nonlinear elastic properties of the square network follow the same scaling as the effective Young's modulus, i.e., linearly proportional to the relative density. In contrast, under uniaxial compression, buckling of the fiber segments leads to more significant nonlinearity, as shown in Fig. 3b, where the critical strain for onset of buckling depends on the relative density. Therefore, the elastic behaviors of the square network under tension and compression are drastically different in the nonlinear regime. Remarkably, while the Poisson's ratio remains zero under tension ($\theta = 0$ and 90°), the cooperative buckling pattern (see inset in Fig. 3b) suggests a negative Poisson's ratio under compression in the nonlinear regime. Moreover, the nonlinear elastic behavior of the square networks also depends on the loading direction (Fernandes et al., 2021). As shown in Fig. 3c, where the stress is normalized by the effective Young's modulus for $\theta = 45^\circ$ in Eq. (5), the square networks stiffen

significantly with the increasing strain under uniaxial tension in the direction of $\theta = 45^{\circ}$, signaling a transition from bending to stretch dominated fiber deformation as the fibers rotate toward the loading direction. Under compression, the fibers rotate toward the transverse direction, leading to a softening behavior, as shown in Fig. 3d. We note that long-wave buckling modes are possible in the periodic networks under compression (Gong et al., 2005; Fernandes et al., 2021), whereas the present study focuses on the cases of uniaxial tension and no long-wave modes were observed in our simulations.

Next, for the triangular and Kagome networks (Fig. 1, b and c), while the effective elastic properties are isotropic in the linear regime, it is found that their nonlinear elastic behaviors are highly anisotropic. Fig. 4 shows the effective stress–strain and strain-strain diagrams for the Kagome networks under uniaxial tension in the two perpendicular directions, i.e., the *x* and *y* directions (horizontal and vertical in Fig. 1); similar results were obtained for the triangular networks (not shown). When stretched in the *x* direction, the load is carried primarily by the fibers parallel to the *x* direction, and the stress–strain behavior (Fig. 4a) is slightly nonlinear, similar to that of the square networks (Fig. 3a), but the Poisson's ratio is different as shown in Fig. 4b. The Poisson's ratio is 1/3 for the triangular and Kagome networks in the linear regime but becomes slightly larger in the nonlinear regime (due to bending of fibers). In contrast, very different nonlinear elastic behaviors are predicted for the Kagome/triangular networks under uniaxial tension in the *y* direction. The effective stress–strain diagrams (Fig. 4c) are initially linear but become much more compliant beyond a small critical strain that depends on the relative density. Subsequently, the stress–strain diagram stiffens and the tangent modulus approaches the initial modulus at relatively large strains. Meanwhile, the lateral strain undergoes a similar transition from the initial Poisson's effect in the linear regime to much larger lateral contractions in the nonlinear regime (Fig. 4d). In this case, the transition from linear to nonlinear behavior is a result of buckling of the fibers in the lateral direction. Fig. 5 shows the deformation patterns of a Kagome network before and after buckling. Evidently, the lateral buckling effectively reduces the axial stiffness in the *y*-direction and increases the lateral contraction of the Kagome network. We note that the stress–strain behaviors in Fig. 4 are independent of the computational box size and no long-wave modes were observed in our simulations of uniaxial tension (from a single unit cell to a maximum of 50 by 50 unit cells). In contrast, long-wave buckling modes are possible in the periodic networks under compression (Gong et al., 2005; Fernandes et al., 2021).

The critical strain for the onset of lateral buckling under uniaxial tension in the *y*-direction can be predicted for both the Kagome and triangular networks. Before buckling, the initial Poisson's effect with an effective Poisson's ratio of 1/3 leads to compression of the fibers in the lateral direction. Following the classical Euler buckling analysis, the critical lateral strain for onset of buckling can be written as

$$\epsilon_{xc} = \frac{\pi^2 d^2}{16(KL)^2} = \frac{\pi^2 \rho^2}{16 A^2 K^2} \tag{7}$$

where K is a constant depending on the boundary conditions for each fiber segment in the lateral direction. The corresponding critical strain in the y direction is:

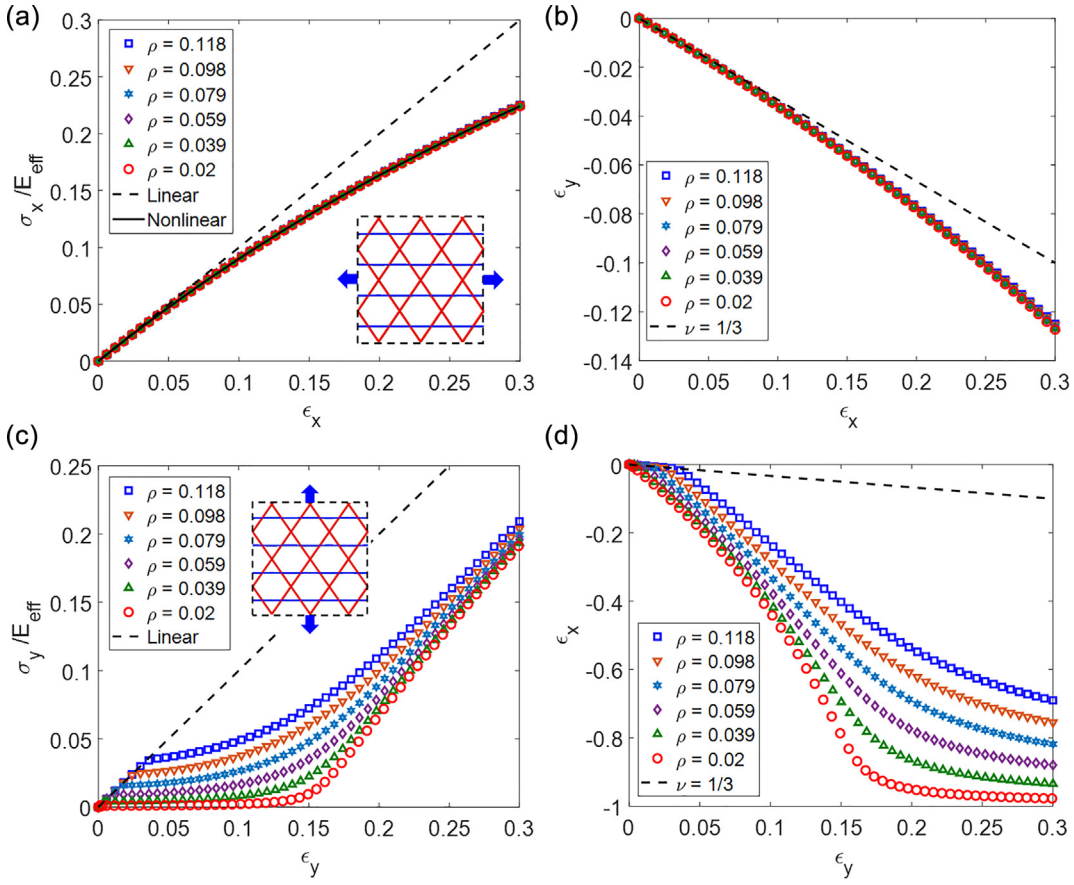

Fig. 4. Effective stress–strain diagrams and lateral strains of Kagome networks under uniaxial tension: (a-b) tension in the *x* direction; (c-d) tension in the *y* direction. The insets in (a) and (c) show the directions of uniaxial tension with respect to the Kagome network.

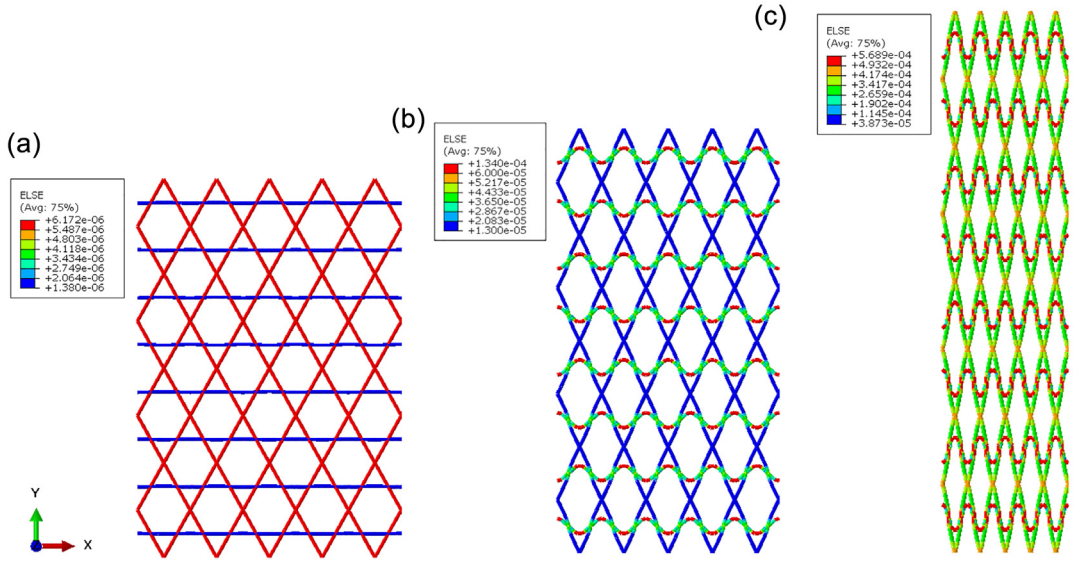

Fig. 5. Deformation patterns of a Kagome network ($\rho = 0.118$) under uniaxial tension in the y-direction: (a) before buckling (regime I, $\epsilon_y = 3\%$); (b) after buckling (regime II, $\epsilon_y = 10\%$); (c) fibers are either nearly aligned or collapsed (regime III, $\epsilon_y = 25\%$). The color scale shows the strain energy density distribution.

$$\epsilon_{yc} = 3\epsilon_{xc} = \beta\frac{\rho^2}{K^2} \tag{8}$$

where $\beta = 1$ for the Kagome networks and $\beta = 1/4$ for the triangular networks. With the same relative density, the aspect ratio of each fiber segment in a Kagome network is half of that in a triangular network. As a result, the critical strain is expected to be higher for the Kagome networks.

Although the joints between the fibers are assumed to be rigid (welded), the joining fibers may rotate together without changing the relative angles at the joints, and thus rotation at the joints is not fully constrained for each fiber segment. Consequently, the constant K in Eq. (8) takes a value between 0.5 for the fully fixed (no rotation) condition and 1 for the pinned (free rotation) condition. By the numerical results as shown in Fig. 6, we found that $K = 0.72$ for the Kagome networks and $K = 0.55$ for the triangular networks. The smaller K for the triangular networks reflects the higher constraint (less rotation) at the joints, due to the higher connectivity (i.e., 3 fibers at each joint versus 2 for the Kagome networks).

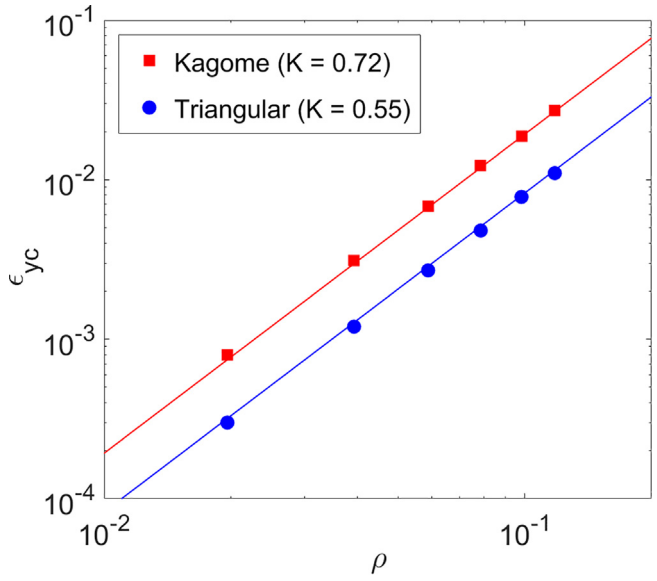

Fig. 6. Critical strain for the onset of lateral buckling in the Kagome and triangular networks under uniaxial tension in the y direction.

To further understand the nonlinear elastic behaviors of the Kagome and triangular networks, we calculate the total strain energy, consisting of fiber stretch, bending and shearing components. In particular, the bending energy provides a measure of the overall bending deformation in the network, which can be used to distinguish stretch- and bending-dominated behaviors (Abhilash et al., 2014; Shahsavari and Picu, 2012). Fig. 7a shows the energy fractions for a Kagome network ($\rho = 0.118$) under uniaxial tension in the y-direction. The shearing component is generally small compared to the stretch and bending components for such a small relative density. Before the critical strain for lateral buckling ($\epsilon_y < \epsilon_{yc}$), the network deformation is stretch dominated (Fig. 5a), similar to a truss network with pin joints. After onset of lateral buckling, the fraction of bending energy increases rapidly and exceeds the fraction of stretch energy. Thus, the network deformation becomes bending dominated, where the lateral buckling allows the fibers in the other two directions to rotate toward the loading direction with little increase in fiber stretch (Fig. 5b). The lateral buckling and fiber rotation together lead to a reduced effective stiffness in the y direction and a much larger Poisson's effect for lateral contraction. The transition from the stretch dominated behavior in the linear regime to the bending dominated behavior can be defined based on the energy fractions, when the fraction of the bending energy first surpasses the fraction of the stretch energy (e.g., $\epsilon_{y1} \approx 0.06$ in Fig. 7a). By this definition, the transition strain is slightly larger than the critical strain for the onset of lateral buckling.

Beyond the first transition strain ($\epsilon_y > \epsilon_{y1}$), the fraction of the bending energy first increases and then decreases, dropping below the fraction of the stretch energy at a relatively large strain (e.g., $\epsilon_{y2} \approx 0.22$ in Fig. 7a). Thereafter, the network deformation transitions back to being stretch-dominated (Fig. 5c), when the fibers are either nearly aligned in the loading direction or fully collapsed by lateral buckling. This explains the stiffening in the stress–strain diagrams (Fig. 4c) and saturation of the lateral strain (Fig. 4d). Therefore, three regimes can be identified for the elastic behaviors of the Kagome and triangular networks under uniaxial tension in the y-direction: (I) Stretch dominated linear regime at small strains

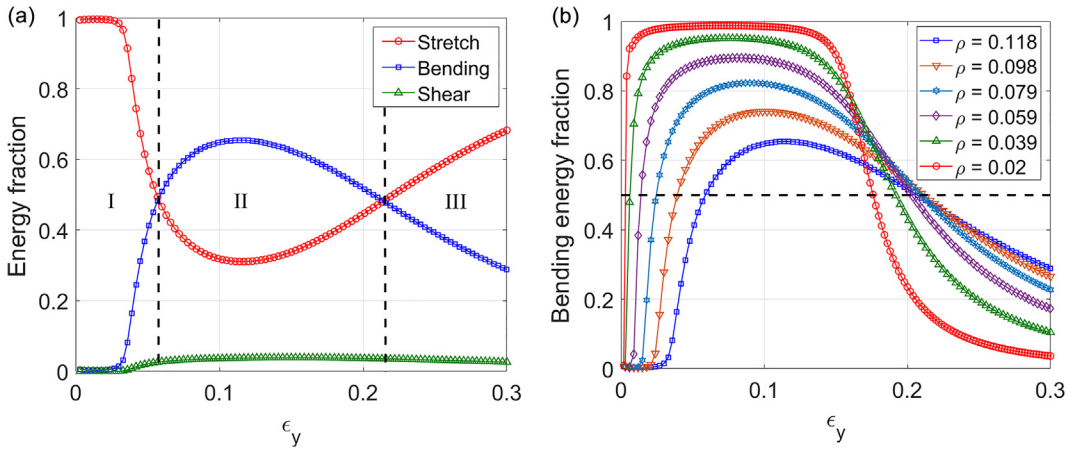

Fig. 7. (a) Evolution of the energy fractions in a Kagome network ($\rho = 0.118$) under uniaxial tension in the y direction; (b) Fraction of the bending energy in Kagome networks with different relative densities. The horizontal dashed line in (b) indicates the bending energy fraction at 50%, and the two transitions are observed for each case as the bending energy fraction crosses the horizontal line as the strain increases, first from below to above 50% and then back to below 50%.

($\epsilon_y < \epsilon_{y1}$), (II) bending dominated regime at intermediate strains ($\epsilon_{y1} < \epsilon_y < \epsilon_{y2}$), and (III) stretch-dominated regime at large strains ($\epsilon_y > \epsilon_{y2}$).

The transition strains for the Kagome and triangular networks depend on the relative density. Fig. 7b shows the fraction of bending energy for Kagome networks with different relative densities; similar results were obtained for triangular networks (not shown). For each relative density, the two transition strains can be determined by setting the fraction of bending energy to be 0.5, and they are shown in Fig. 8. Similar to the critical strain for lateral buckling, the first transition strain approximately scales with the relative density as: $\epsilon_{y1} \sim \rho^2$. In contrast, the second transition strain increases slowly with the relative density. Consequently, the bending dominated regime expands as the relative density decreases. For the lowest relative density ($\rho = 0.02$) considered for the Kagome networks, the first transition strain is <0.01 and the fraction of bending energy is close to 1 for a significant portion of the bending-dominated regime II before it transitions to stretch-dominated regime III (see Fig. 7b).

Two types of transitions may be noted in Fig. 8 for both the Kagome and triangular networks. First, at a small strain (e.g., $\epsilon_y = 0.01$), the network deformation transitions from the stretch-dominated regime I to the bending-dominated regime II as the relative density decreases (as indicated by the horizontal arrows in Fig. 8), similar to that predicted for random fiber networks (Wu and Dzenis, 2005; Broedersz et al., 2012; Shahsavari and Picu, 2012; Ban et al., 2016). Second, for a relatively low density (e.g., $\rho = 0.06$), the network deformation transitions from the bending-dominated regime II to the stretch-dominated regime III as the strain increases (as indicated by the vertical arrows in Fig. 8), similar to strain stiffening as predicted for random fiber networks (Onck et al., 2005; Huisman et al., 2007; Broedersz et al., 2008; Islam and Picu, 2018). Remarkably, these transitions occur despite the infinitely long fibers in the periodic networks.

3. Random 2D networks

To construct a random 2D network model, a square representative area element (RAE) was used, within which long, straight fibers of random orientations were placed at random seed points, with each fiber terminating on the edges of the square element. To control the relative density of the random network, we define the line density as the total length of all fibers (L_{all}) per unit area, namely,

$$\rho_L = \frac{L_{\text{all}}}{L_{\text{RAE}}^2} \tag{9}$$

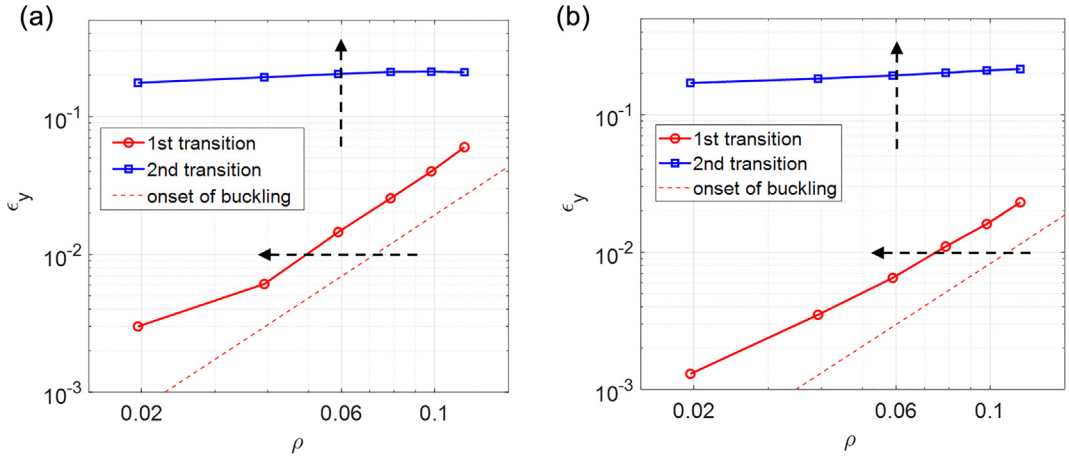

Fig. 8. Transition strains versus the relative density for (a) Kagome and (b) triangular networks. The horizontal and vertical arrows indicate two types of transitions as the relative density and the strain changes, respectively.

where L_{RAE} is the side length of the square element. Fibers were added to the element until the desired line density was reached within a small tolerance (<0.1%). The seed points and orientations of the fibers follow simple uniform distributions. In this process, the line density and the fiber diameter can be independently controlled. The relative density of the 2D network is proportional to the product of the line density and the fiber diameter, namely,

$$\rho = \alpha \rho_L d \tag{10}$$

where $\alpha = \frac{\pi}{4}$ for fibers with a circular cross section; the same is true for both the periodic and random 2D networks.

Unlike the periodic networks with a single segment length, the fiber segment length (L_s) in a random network is statistically distributed. As a result, to represent the statistical distribution of the segment lengths, the size of the RAE must be sufficiently large compared to the average segment length, i.e., $L_{RAE} \gg \langle L_s \rangle$, following the concept of separation of scales (Ostoja-Starzewski, 2006). The average segment length in a 2D fiber network is inversely proportional to the line density, i.e., $\langle L_s \rangle \sim \rho_L^{-1} \sim d/\rho$, for both the random and periodic 2D networks (Picu, 2011). In this study, we take $L_{RAE} \approx 50\langle L_s \rangle \sim 50d/\rho$, which is much larger than the fiber diameter for a low relative density ($\rho < 0.12$). For a given fiber diameter, the RAE size increases as the relative density decreases. As an example, for a network of Ge nanowires with $d =$ 50 nm (Smith et al., 2010), the RAE size is about 25 μm (500 times the fiber diameter) for a relative density of 0.1. Alternatively, for a given line density (ρ_L) and the network topology, the relative density can be varied by changing the fiber diameter according to Eq. (10). The choice of the RAE size will be discussed further following a statistical analysis in order to quantify the precision in the effective elastic properties of the 2D random networks.

The porosity of a random 2D network can be defined as the volume ratio of the space not occupied by the fibers, namely:

$$\phi = 1 - \rho \tag{11}$$

The average pore size is proportional to the average segment length, i.e., $\langle L_p \rangle \sim \langle L_s \rangle \sim d/\rho$, which is inversely proportional to the relative density.

3.1. Structural properties: Statistics and scaling

Consider two key structural properties of the random 2D networks: the fiber segment length (L_s) and the number density of joints (ρ_J). For each RAE (see Fig. 1d), the fiber segment lengths between neighboring joints vary statistically and the average segment length is calculated. For a given relative density, a large number of RAEs were generated and the histogram of the average segment length is shown in Fig. 9a (for $\rho = 0.118$). The inset of Fig. 9a shows the exponential distribution of the segment lengths in one realization, similar to the 3D random networks generated by Kim et al. (2009) and Zagar et al. (2011), although generation of the random networks in 3D is more complicated. The ensemble average of the segment lengths among a large number of RAEs depends on the relative density as shown in Fig. 9b. As expected,

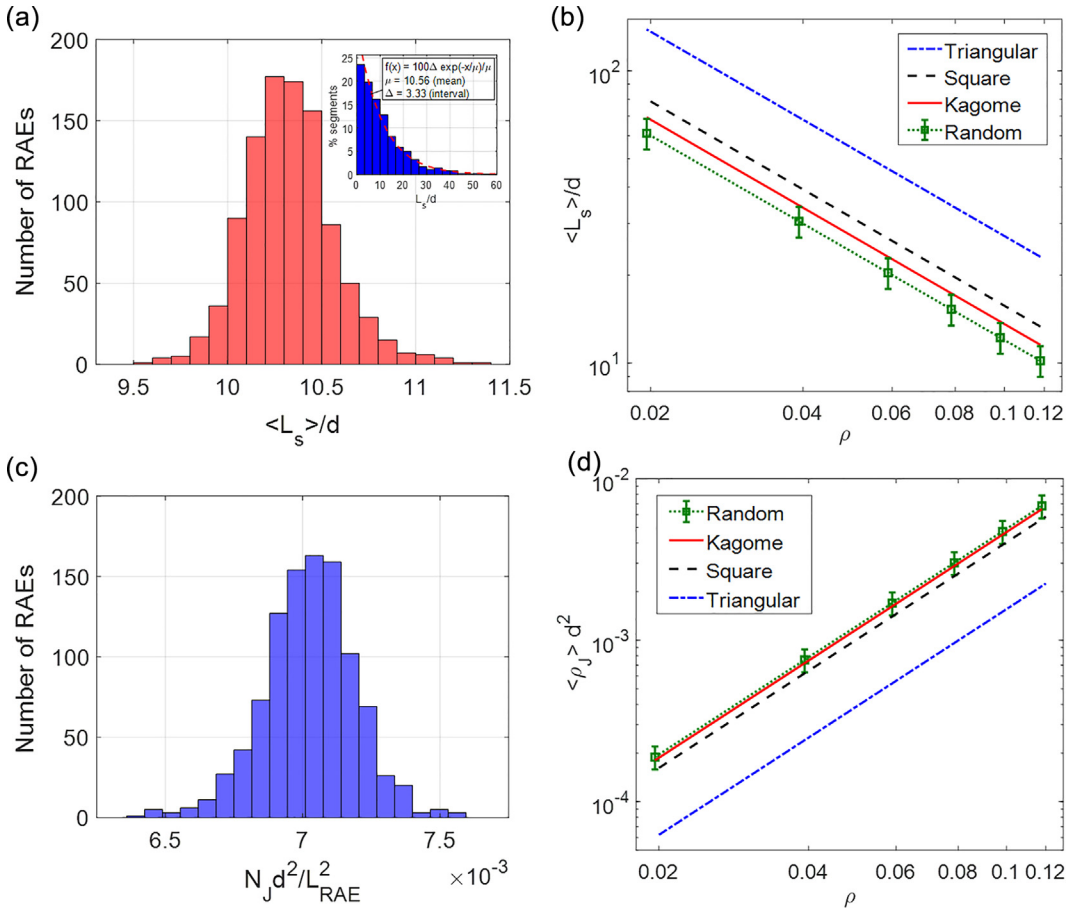

Fig. 9. (a) Histogram of the normalized average fiber segment lengths in 1000 RAE realizations of the random 2D network with the relative density $\rho = 0.118$ ($\rho_L L_{RAE} = 50, d/L_{RAE} = 0.003$). The inset shows the exponential distribution of the segment lengths in one realization. (b) The normalized average segment length vs the relative density. (c) Histogram of the normalized number density of joints in the 1000 RAEs. (d) Average number density of joints vs the relative density in both random and periodic 2D networks. The error bars in (b) and (d) show the standard deviations among the 1000 RAE realizations of the random networks.

the ratio, $\langle L_s \rangle / d$, is inversely proportional to the relative density, qualitatively similar to the periodic 2D networks. Following Eq. (1), we write

$$\frac{\langle L_s \rangle}{d} = A\rho^{-1} \tag{12}$$

where $A \approx 1.2$ is obtained for the random 2D networks, in close agreement with the prediction by Kallmes and Corte (1960). Recall that $A = \pi/2$ for the square networks, $A = \sqrt{3}\pi/2$ for the triangular networks, and $A = \sqrt{3}\pi/4$ for the Kagome networks (Table 1). Apparently, in terms of the average segment length, the random 2D networks are closest to the Kagome networks.

Taking $\rho_L L_{\mathrm{RAE}} = 50$ in construction of the random 2D network model, the ratio between L_{RAE} and the average segment length is then: $\frac{L_{\mathrm{RAE}}}{\langle L_s \rangle} = \frac{\alpha}{A}\rho_L L_{\mathrm{RAE}} = 32.7$, which is considered sufficiently large for the RAE to be statistically representative. The relative density is then varied by changing the ratio d/L_{RAE} following Eq. (10). We note that the ratio between L_{RAE} and the fiber diameter is: $\frac{L_{\mathrm{RAE}}}{d} = \alpha\rho^{-1}(\rho_L L_{\mathrm{RAE}}) = 39\rho^{-1}$ for $\rho_L L_{\mathrm{RAE}} = 50$. This ratio ($L_{\mathrm{RAE}}/d$) in the present study ranges from 330 to 1950, which is larger than those in previous works (Dirrenberger et al., 2014; Chatti et al., 2020) for 3D random networks.

The number density of joints (per unit area) in a periodic 2D network is inversely proportional to the square of the segment length, i.e., $\rho_J \sim L_s^{-2} \sim \rho^2 d^{-2}$. For random 2D networks, the number of joints (N_J) varies statistically among a large number of RAEs, and Fig. 9c shows the histogram of the number of joints for 1000 RAEs with the same relative density ($\rho = 0.118$). It is found that the average number density of joints follows the same scaling as the periodic networks as shown in Fig. 9d, namely

$$\langle \rho_J \rangle = \frac{\langle N_J \rangle}{L_{RAE}^2} = A_J \frac{\rho^2}{d^2} \tag{13}$$

where $A_J = 0.485$ is obtained for the random 2D networks. For comparison, $A_J = 1/A^2 = 0.405$ for the square networks, $A_J = 2/(\sqrt{3}A^2) = 0.156$ for the triangular networks, and $A_J = \sqrt{3}/(2A^2) = 0.468$ for the Kagome networks. Again, the random 2D networks are closest to the Kagome networks in terms of the average number density of joints. For the same relative density and the fiber diameter, the number density of joints depends on the joint connectivity (i.e., the number of fibers at each joint). The joint connectivity is 2 for the square and Kagome networks, and it is 3 for the triangular network. As a result, the triangular network has the lowest number density of joints. The joint connectivity for the random 2D networks is approximately 2, similar to the square and Kagome networks.

3.2. Elastic properties

Similar to the periodic 2D networks, finite element simulations were conducted to study the elastic behavior of the random 2D networks under uniaxial tension. The fibers were modeled using the Timoshenko beam elements (B22), and the fiber material was assumed to be isotropic and linearly elastic in terms of the Cauchy stress and the logarithmic strain. Unlike the periodic networks, the boundary conditions for the RAE of random 2D networks were aperiodic. Instead, the displacement along the edges of each RAE is constrained such that the edges remain straight during deformation. Essentially, we assume that the deformation of a large random network is affine down to the scale of the RAE (mesoscale) but may become non-affine microscopically within the RAE. Moreover, for a given relative density, there are many possible network structures as a result of the random realization of RAE. Thus, the elastic properties in general vary statistically among different RAE realizations, and the averaged properties over a large number of RAEs are most relevant for potential applications at scales much larger than L_{RAE}. A statistical analysis is necessary to estimate the relative errors that depend on both the RAE size and the number of random realizations (Kanit et al., 2003; Dirrenberger et al., 2014).

First, we simulated the random 2D networks by using one particular RAE realization (Fig. 1d) with the same line density (ρ_L) and joint connectivity but varying the fiber diameter (d) to obtain different relative densities (recall that $\rho \sim \rho_L d$). Fig. 10a shows the stress–strain diagrams under uniaxial tension in the y-direction, whereas Fig. 10b shows the lateral strain versus the axial strain. For the purpose of comparison, the effective stress is normalized in Fig. 10a by the effective Young's modulus of the corresponding Kagome network with the same relative density (Eq. (2)). For all the relative densities considered, the elastic responses are similar under uniaxial tension in the x-direction (not shown), indicating an essentially isotropic behavior as expected for a statistically representative RAE. Compared to the linearly elastic responses predicted for the periodic 2D networks shown as the straight lines in Fig. 10a, the random 2D networks are generally more compliant even at infinitesimal strains. The axial stress–strain response of the random 2D network is slightly nonlinear, with no clear transition from linear to nonlinear regimes. Unlike the previous studies of 2D and 3D random networks with short fibers (Onck et al., 2005; Huisman et al., 2007; Broedersz et al., 2008; Islam and Picu,

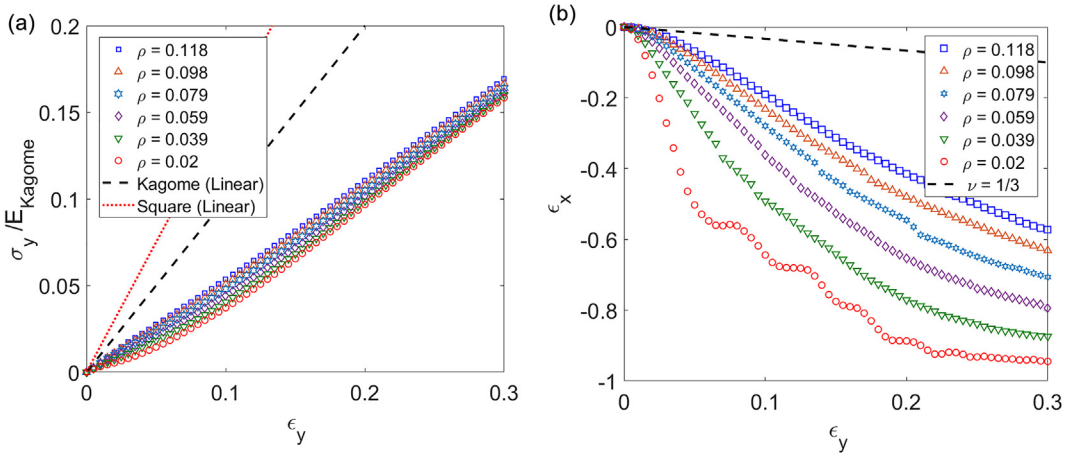

Fig. 10. (a) Effective stress–strain diagrams and (b) lateral strain responses of random 2D networks under uniaxial tension in the y-direction.

2018), Fig. 10a shows no significant strain stiffening. In contrast, the lateral strain responses in Fig. 10b are highly nonlinear, similar to those in Fig. 4d for the Kagome networks subject to uniaxial tension in the y-direction. It is noted that, while the lateral strain response of the Kagome network is linear up to a critical strain for buckling, the random networks do not show a clear transition from the linear to nonlinear lateral strain responses. Fig. 11 shows the simulated deformations of the random 2D network with the relative density $\rho = 0.118$. Evidently, there is considerable buckling of the fiber segments even at a relatively small strain (3%). Similar to the Kagome network (Fig. 5), the uniaxial tension leads to lateral contraction and thus buckling of the fibers in the lateral direction. While the onset of lateral buckling in the periodic Kagome network occurs cooperatively at a well-defined critical strain, the buckling in the random network occurs stochastically and continuously with no obvious critical strain. Since the segment lengths are statistically distributed within one RAE (Fig. 9a inset), the long segments close to the lateral direction are likely to buckle first. As the axial strain increases, more segments buckle, leading to more lateral contraction. Meanwhile, due to the random fiber orientations, there are a few fibers oriented in the direction close to the loading direction and they seem to dominate the axial stress–strain behavior. The other fibers are either buckled or rotated towards the loading direction, without contributing significantly to the overall stiffness. Clearly, the deformation within the RAE is largely non-affine except for a few nearly aligned fibers.

To shed more insight into the elastic behaviors of the random 2D networks, we calculated the energy fractions during deformation as shown in Fig. 12a. Unlike the Kagome network in Fig. 7a, the stretch energy remains dominant (>80%) in the random 2D network throughout the deformation, and there is no transition from stretch to bending dominated regime for the random 2D network. Despite all the buckling fibers in Fig. 11, the fraction of the bending energy is fairly low (<20%). The strain energy distributions in Fig. 11 show that most of the strain energy is stored in the fibers oriented close to the loading direction and they are primarily being stretched. This behavior is in sharp contrast with short-fiber random networks (Onck et al., 2005; Huisman et al., 2007; Broedersz et al., 2008; Islam and Picu, 2018), where a transition from bending to stretch dominated deformation leads to significant strain stiffening. Fig. 12b compares the fractions of bending energy in the random 2D networks with different relative densities. The maximum fraction increases slightly with decreasing relative density, but remains low (<25%). Hence, the deformation of the random 2D network of long fibers remains stretch-dominated for the range of the relative density considered here.

We have noted that the stress–strain behavior in Fig. 10a appears to be different from previous studies of random networks (e.g., Onck et al., 2005; Huisman et al., 2007; Wang et al., 2014; Islam and Picu, 2018), with no significant strain stiffening and no transition from bending to stretch dominated behavior. There are at least two differences between the present study and the previ-

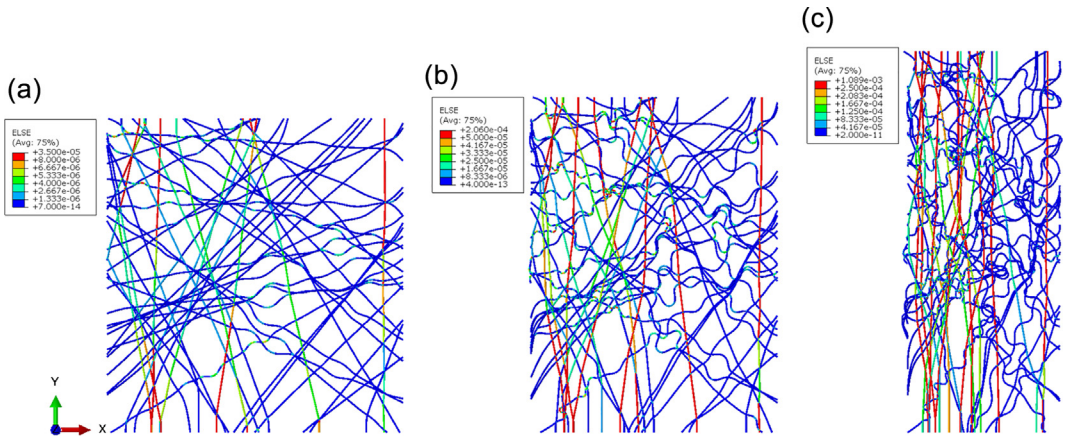

Fig. 11. Simulated deformations of a random 2D network ($\rho = 0.118$, undeformed in Fig. 1d) under uniaxial tension in the y-direction with increasing strain: (a) 3%; (b) 10%; (c) 25%. The color scale shows the strain energy density distribution.

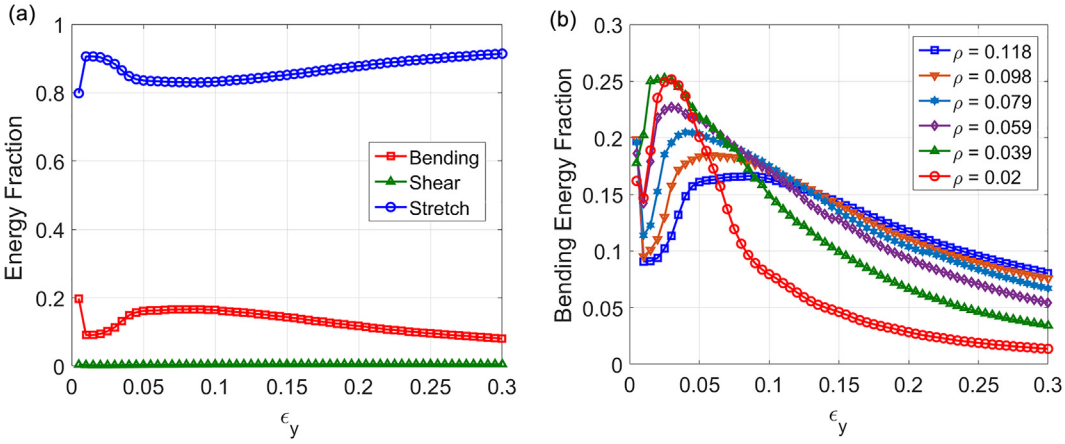

Fig. 12. (a) Energy fractions versus the strain for a random 2D network ($\rho = 0.118$) under uniaxial tension; (b) Variation of the bending energy fraction for random 2D networks of different relative densities.

ous works that may lead to the different behavior: (i) While many of the previous works considered relatively short fiber lengths compared to the cell size (or in terms of the fiber length/diameter ratio), the present study considers a limiting case of infinitely long fibers (or fiber length much greater than the fiber diameter and the segment length); (ii) While some of the previous studies considered simple shear with a macroscopic volumetric constraint, the present study focuses on the uniaxial tension with no volumetric constraint.

As noted in the previous works (Onck et al., 2005; Wang et al., 2014; Islam and Picu, 2018), the rotation and alignment of the fibers along the principal loading direction led to the transition from bending to stretch dominated behavior and hence strain stiffening. In contrast, for the random 2D networks with long fibers, there are always a few fibers oriented close to the principal loading direction (under uniaxial tension), and these fibers form primary stress paths connecting the opposite faces of the model, carrying most of the applied load from the beginning with little rotation. As shown in Fig. 11, these fibers have the largest strain energy density and thus dominate the uniaxial stress–strain behavior (with little stiffening). This behavior is also consistent with the stress–strain behaviors of the Kagome networks (Fig. 4), where there is no stiffening under uniaxial tension in the x-direction (Fig. 4a) but there is strain stiffening in the y-direction (Fig. 4c), because the fibers in the x-direction dominate the behavior in the former case, but with no fibers oriented in the y-direction, buckling and rotation of the fibers lead to strain stiffening in the y-direction. Similarly, for the square networks, there is no stiffening under uniaxial tension in the x or y-direction (Fig. 3a) but there is significant strain stiffening under uniaxial tension with $\theta = 45^{\circ}$ (Fig. 3c).

To examine the effect of volumetric constraint, we have also conducted simulations of the random 2D networks under biaxial deformation with a constraint on the area of the RAE and found that the effective shear stress–strain response does exhibit some level of strain stiffening, more so than the case of uniaxial tension in Fig. 10. However, the strain stiffening appears to be less significant compared to some of the previous works (e.g., Onck et al., 2005), which we believe is due to the effects of the long fiber length and the kinematic constraints with the crosslinks along each fiber. As noted by Islam and Picu (2018), additional constraints are imposed through crosslinking along each fiber in the fibrous networks, and as a result, fiber re-orientation is more difficult and strain stiffening is reduced.

We compare the uniaxial stress–strain behavior of the random 2D networks with that of the Kagome networks in Fig. 13. For the same relative density, the random network is more compliant at both small and large strains. At intermediate strains, however, when the deformation of the Kagome network is bending dominated, it becomes more compliant than the random network. This difference can be directly correlated to the buckling behaviors. For the Kagome networks, cooperative buckling of all lateral segments leads to drastically lower stiffness in the bending dominated regime. For the random 2D networks, however, stochastic buckling occurs in a continuous fashion with little effect on the axial stiffness, but leading to a large Poisson's effect for the lateral strain response (Fig. 10b).

Next, the elastic responses of different RAEs of the random 2D networks were simulated. For each relative density, we simulated 100 RAEs and calculated the effective Young's modulus (E_{eff}) and Poisson's ratio (ν_{eff}), both evaluated as the secant moduli at a relatively small strain of 0.01 for the network deformation. The statistical distributions of the effective elastic properties are shown in Fig. 14 (a and c). We observe considerable variances in both E_{eff} and ν_{eff} among the RAEs for the random network of the same relative density, which may be expected from the statistical nature of

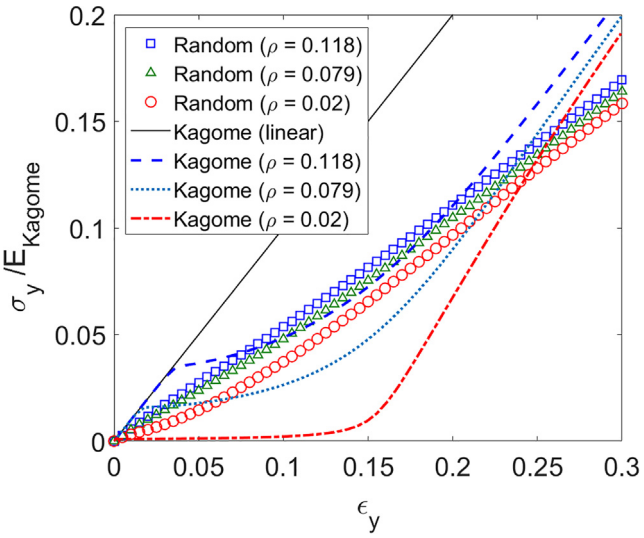

Fig. 13. Comparison of the uniaxial stress–strain responses between the random 2D networks and the Kagome networks.

the random networks with different network structures in terms of the segment lengths and the number of joints for different random realizations as shown in Fig. 9. The mean values of these effective elastic properties are shown as functions of the relative density (Fig. 14, b and d). For comparison, the effective Young's modulus and Poisson's ratio of the Kagome and triangular networks (at the same strain of 0.01) are also shown. Interestingly, Fig. 14b shows that the effective Young's moduli of the periodic networks transition from bending dominated ($E_{\text{eff}} \sim \rho^3$) to stretch dominated ($E_{\text{eff}} \sim \rho$) as the relative density increases. Since the effective Young's moduli are evaluated at an axial strain of 0.01, the periodic networks of higher density have not reached the critical strain for onset of cooperative buckling so that the elastic responses are stretch dominated ($E_{\text{eff}} \sim \rho$). For periodic networks of lower density, the critical strain for buckling is lower than 0.01 and thus the elastic responses become bending dominated ($E_{\text{eff}} \sim \rho^3$), as noted in Fig. 8. Due to different critical strains for the Kagome and triangular networks (Fig. 6), the critical relative density values for the transition are also different between the two periodic networks. In contrast, the effective Young's moduli of the random 2D networks do not show such a transition. Instead, they follow a nearly linear scaling with the relative density, $\langle E_{\text{eff}} \rangle \sim \rho^{1.3}$, suggesting primarily stretch-dominated responses for all the relative density values considered here. This result appears to be consistent with the master curve obtained by Shahsavari and Picu (2012) and Shahsavari and Picu (2013) for the random 2D networks at the limit of infinitely long fibers. On the other hand, the effective Poisson's ratios in Fig. 14d show similar transitions for both the periodic and random 2D networks. The Poisson's ratio is 1/3 for the periodic networks before buckling (for higher relative density) and increases significantly after buckling (for lower relative density). For the random 2D networks, the average Poisson's ratio is slightly below 1/3 for those with a higher relative density and also increases significantly for those with a lower relative density. This suggests that, while the effective Young's modulus is primarily stretch dominated for the random 2D networks, the effective Poisson's ratio does show a transition to bending dominated behavior as the relative density decreases. As noted in Fig. 11, although the stochastic buckling in the random 2D networks does not contribute significantly to the axial stress–strain behavior, it is significant for the lateral contraction and hence the

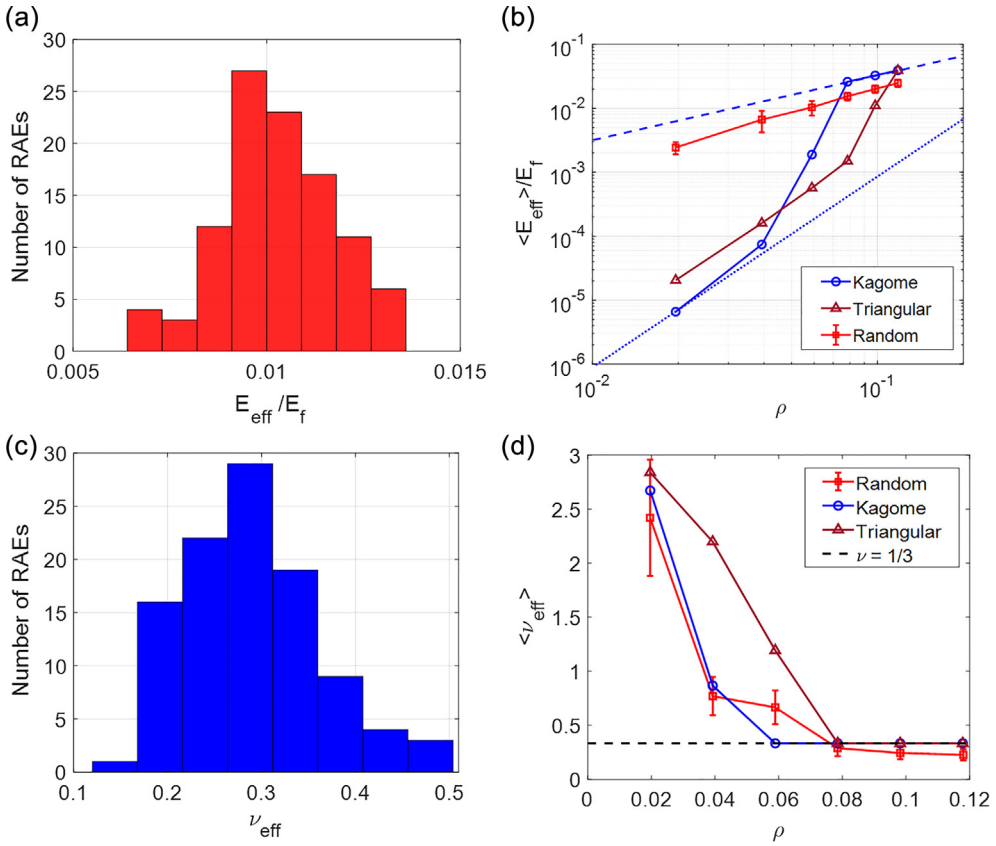

Fig. 14. (a) Histogram of the normalized effective Young's modulus in 100 RAEs of the random 2D network with the relative density $\rho = 0.118$; (b) Average effective Young's modulus versus the relative density; The dashed and dotted straight lines indicate the linear (stretch dominated) and cubic (bending dominated) scaling relations, respectively. (c) Histogram of the effective Poisson's ratio of the random 2D network; (d) Average effective Poisson's ratio versus the relative density. The error bars in (b) and (d) show the standard deviations among the 100 RAE realizations for each relative density of the random network.

effective Poisson's ratio. The unusually large values of the effective Poisson ratio ($\nu_{eff} > 1$), which have been reported previously in soft fibrous networks (Kabla and Mahadevan, 2007; Islam and Picu, 2018; Ban et al., 2019), are indicative of the largely non-affine deformations in the RAEs with significant bending or buckling of the fibers.

It has been shown that a proper representative volume element (RVE) size for random 3D networks of long fibers can be associated with a given precision of the estimation of the effective property and the number of realizations (Kanit et al., 2003; Dirrenberger et al., 2014). Similarly, for the random 2D networks, the statistical method in the previous works (Kanit et al., 2003; Dirrenberger et al., 2014) can be adopted to estimate the proper RAE size and associated precision for the effective elastic properties. Fig. 15 shows the effective Young's modulus and Poisson's ratio obtained from RAEs of different sizes. Note that the RAE size (L_{RAE}) normalized by the line density (ρ_L) is proportional to the ratio between L_{RAE} and the fiber diameter (d), i.e., $\rho_L L_{RAE} = \frac{\rho}{\alpha}\frac{L_{RAE}}{d}$, which depends

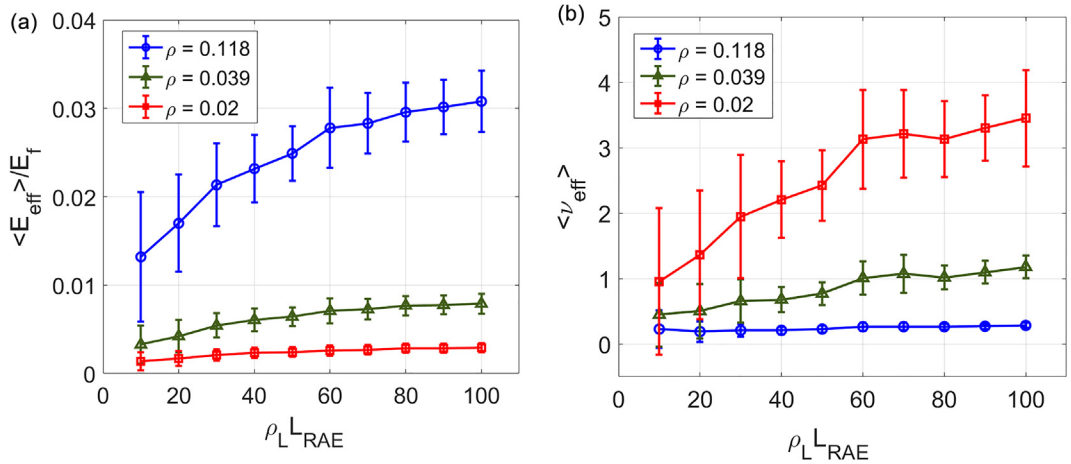

Fig. 15. Effect of RAE size on the effective elastic properties of the random 2D networks. (a) Young's modulus, and (b) Poisson's ratio. The error bars show the standard deviations among the 100 RAE realizations for each case.

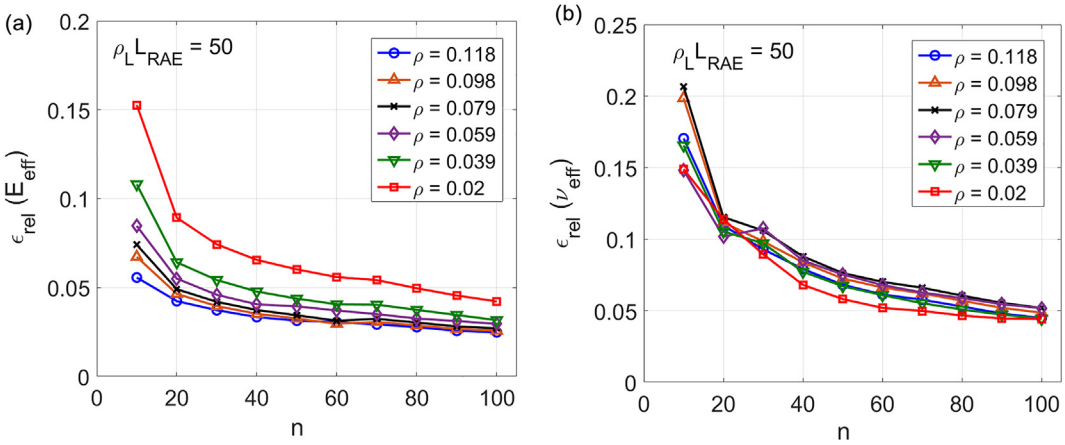

Fig. 16. Relative errors for (a) the effective Young's modulus and (b) Poisson's ratio of random 2D networks.

on the relative density (ρ). The ratio $\frac{L_{RAE}}{d}$ in Fig. 15 ranges from 66 in the case of $\rho_L L_{RAE} = 10$ and $\rho = 0.118$ to 3927 in the case of $\rho_L L_{RAE} = 100$ and $\rho = 0.02$. For each RAE size, 100 random realizations were used to calculate the average properties and the standard deviations for each relative density. The average values of Young's modulus and Poisson's ratio increase with the increasing RAE size, while the standard deviations decrease. Both the average values and the standard deviation appear to be converging (but not fully converged), with non-vanishing standard deviation due to the statistical nature of the random networks. Following the statistical method (Kanit et al., 2003; Dirrenberger et al., 2014), the relative error in the estimation of the effective properties with a large number of random realizations can be calculated as

$$\epsilon_{rel}(L_{RAE}, n) = \frac{2s}{\mu\sqrt{n}} \tag{14}$$

where n is the number of RAE realizations of the same size (L_{RAE}), μ is the average property and s is the standard deviation. Taking $\rho_L L_{RAE} = 50$, the relative errors for the effective Young's modulus and Poisson's ratio are shown in Fig. 16. As the number of realizations increases, the relative errors decrease as expected. With $n = 100$, the relative errors are around 5% or lower for both the Young's modulus and Poisson's ratio. With a larger RAE size (e.g., $\rho_L L_{RAE} = 100$) and $n = 100$, the relative errors drop slightly to around 4%. Therefore, a proper RAE size can be used along with a large number of random realizations to estimate the effective elastic properties of the random 2D networks for a given precision.

4. Summary

In this study, we numerically simulated the nonlinearly elastic responses of low-density 2D networks of crosslinked long fibers, including both periodic and random networks. A comparison between the periodic and random 2D networks highlights the profound effects of the network topology on the effective elastic properties as summarized below.

- The structural properties such as the average segment length and the number density of joints (crosslinks) follow similar scaling laws for the periodic and random 2D networks. For random 2D networks, a large number of statistically representative elements are used to determine the average structural properties.
- The square networks are anisotropic in both the linear and nonlinear regimes, whereas the triangular and Kagome networks are isotropic in the linear regime but becomes anisotropic in the nonlinear regime. The random 2D networks are statistically isotropic in both the linear and nonlinear regimes.
- For low-density triangular and Kagome networks, cooperative buckling of the fiber segments could take place at small strains, leading to nonlinear, anisotropic elastic behaviors. As a result, a transition from stretch dominated to bending dominated deformation is predicted as the strain increases (strain softening). A second transition from the bending dominated to stretch dominated deformation with strain stiffening occurs at a larger strain.
- For the random 2D networks of long fibers, the axial stress–strain behavior is statistically isotropic and slightly nonlinear, primarily stretch dominated. Meanwhile, stochastic buckling occurs continuously in the random networks, leading to significant lateral contraction. Consequently, while the effective Young's modulus follows a nearly linear scaling with respect to the relative density, the effective Poisson's ratio exhibits a transition from stretch to bending dominated behavior as the relative density decreases.
- Finally, following the statistical method, a given precision can be achieved with small relative errors ($\epsilon_{rel} < 5\%$) in the estimation of the effective elastic properties of the random 2D networks by using a proper RAE size along with a sufficiently large number of random realizations.

Declaration of Competing Interest

The authors declare that they have no known competing financial interests or personal relationships that could have appeared to influence the work reported in this paper.

Acknowledgments

We gratefully acknowledge funding of this work by the Center for Dynamics and Control of Materials (CDCM) supported by the National Science Foundation (NSF) under Award No. DMR-1720595. Discussions with Dr. Brian Korgel and Taizhi Jiang regarding the synthesis and structural characterization of Ge nanowire aerogels were helpful.

References

Abhilash, A.S., Baker, B., Trappmann, B., Chen, C., Shenoy, V., 2014. Remodeling of fibrous extracellular matrices by contractile cells: predictions from discrete fiber network simulations. Biophys. J. 107 (8), 1829–1840.

Åström, J.A., Kumar, P.B.S., Vattulainen, I., Karttunen, M., 2008. Strain hardening, avalanches, and strain softening in dense cross-linked actin networks. Phys. Rev. E 77 (5), 051913. https://doi.org/10.1103/PhysRevE.77.051913.
Ban, E., Barocas, V.H., Shepard, M.S., Picu, R.C., 2016. Softening in random network of non-identical beams. J. Mech. Phys. Solids 87, 38–50.
Ban, E., Franklin, J.M., Nam, S., Smith, L.R., Wang, H., Wells, R.G., Chaudhuri, O., Liphardt, J.T., Shenoy, V.B., 2018. Mechanisms of plastic deformation in collagen networks induced by cellular forces. Biophys. J. 114 (2), 450–461.
Ban, E., Wang, H., Franklin, J.M., Liphardt, J.T., Janmey, P.A., Shenoy, V.B., 2019. Strong triaxial coupling and anomalous Poisson effect in collagen networks. Proc. Natl. Acad. Sci. 116 (14), 6790–6799.
Broedersz, C.P., MacKintosh, F.C., 2014. Modeling semiflexible polymer networks. Rev. Mod. Phys. 86 (3), 995–1036. https://doi.org/10.1103/RevModPhys.86.995.
Broedersz, C.P., Sheinman, M., MacKintosh, F.C., 2012. Filament-length-controlled elasticity in 3D fiber networks. Phys. Rev. Lett. 108, (7). https://doi.org/10.1103/PhysRevLett.108.078102 078102.
Broedersz, C.P., Storm, C., MacKintosh, F.C., 2008. Nonlinear elasticity of composite networks of stiff biopolymers with flexible linkers. Phys. Rev. Lett. 101 (11), 118103. https://doi.org/10.1103/PhysRevLett.101.118103.
Chatti, F., Bouvet, C., Michon, G., Poquillon, D., 2020. Numerical analysis of shear stiffness of an entangled cross-linked fibrous material. Int. J. Solids Struct. 184, 221–232.
Christensen, R.M., 2000. Mechanics of cellular and other low-density materials. Int. J. Solids Struct. 37 (1-2), 93–104.
Cox, H.L., 1952. The elasticity and strength of paper and other fibrous materials. Br. J. Appl. Phys. 3 (3), 72–79.
Dirrenberger, J., Forest, S., Jeulin, D., 2014. Towards gigantic RVE sizes for 3D stochastic fibrous networks. Int. J. Solids Struct. 51 (2), 359–376.
Fernandes, M.C., Aizenberg, J., Weaver, J.C., Bertoldi, K., 2021. Mechanically robust lattices inspired by deep-sea glass sponges. Nat. Mater. 20 (2), 237–241.
Fleck, N.A., Deshpande, V.S., Ashby, M.F., 2010. Micro-architecture materials: Past, present and future. Proc. R. Soc. A 466, 2495–2516.
Gong, L., Kyriakides, S., Triantafyllidis, N., 2005. On the stability of Kelvin cell foams under compressive loads. J. Mech. Phys. Solids 53 (4), 771–794.
Hall, M.S., Alisafaei, F., Ban, E., Feng, X., Hui, C.-Y., Shenoy, V.B., Wu, M., 2016. Fibrous nonlinear elasticity enables positive mechanical feedback between cells and ECMs. Proc. Natl. Acad. Sci. 113 (49), 14043–14048.
Holmberg, V.C., Bogart, T.D., Chockla, A.M., Hessel, C.M., Korgel, B.A., 2012. Optical properties of silicon and germanium nanowire fabric. J. Phys. Chem. C 116 (42), 22486–22491.
Huisman, E.M., van Dillen, T., Onck, P.R., Van der Giessen, E., 2007. Three-dimensional cross-linked f-actin networks: relation between network architecture and mechanical behavior. Phys. Rev. Lett. 99 (20), 208103. https://doi.org/10.1103/PhysRevLett.99.208103.
Islam, M.R., Picu, R.C., 2018. Effect of network architecture on the mechanical behavior of random fiber networks. J. Appl. Mech. 85, 081011. https://doi.org/10.1115/1.4040245.
Jung, S.M., Jung, H.Y., Dresselhaus, M.S., Jung, Y.J., Kong, J., 2012. A facile route for 3D aerogels from nanostructured 1D and 2D materials. Sci. Rep. 2, 849. https://doi.org/10.1038/srep00849.
Jung, S.M., Jung, H.Y., Fang, W., Dresselhaus, M.S., Kong, J., 2014. A facile methodology for the production of in situ inorganic nanowire hydrogels/aerogels. Nano Lett. 14 (4), 1810–1817.
Kabla, A., Mahadevan, L., 2007. Nonlinear mechanics of soft fibrous networks. J. R. Soc. Interface 4 (12), 99–106.
Kallmes, O., Corte, H., 1960. The structure of paper I. The statistical geometry of an ideal two dimensional fiber network. Tappi J. 43 (9), 737–752.
Kanit, T., Forest, S., Galliet, I., Mounoury, V., Jeulin, D., 2003. Determination of the size of the representative volume element for random composites: statistical and numerical approach. Int. J. Solids Struct. 40 (13-14), 3647–3679.
Kim, T., Hwang, W., Kamm, R.D., 2009. Computational analysis of a cross-linked actin-like network. Exp. Mech. 49 (1), 91–104.
Koh, C.T., Oyen, M.L., 2012. Branching toughens fibrous networks. J. Mech. Behav. Biomed. Mater. 12, 74–82.
Kulachenko, A., Uesaka, T., 2012. Direct simulations of fiber network deformation and failure. Mech. Mater. 51, 1–14.
Meng, Q., Wang, T.J., 2019. Mechanics of Strong and Tough Cellulose Nanopaper. Appl. Mech. Rev. 71 (4), 040801. https://doi.org/10.1115/1.4044018.
Merson, J., Picu, R.C., 2020. Size effects in random fiber networks controlled by the use of generalized boundary conditions. Int. J. Solids Struct. 206, 314–321.
Meza, L.R., Das, S., Greer, J.R., 2014. Strong, lightweight, and recoverable three-dimensional ceramic nanolattices. Science 345 (6202), 1322–1326.
Meza, L.R., Zelhofer, A.J., Clarke, N., Mateos, A.J., Kochmann, D.M., Greer, J.R., 2015. Resilient 3D hierarchical architected metamaterials. PNAS 112 (37), 11502–11507.
Onck, P.R., Koeman, T., van Dillen, T., van der Giessen, E., 2005. Alternative explanation of stiffening in cross-linked semiflexible networks. Phys. Rev. Lett. 95 (17), 178102. https://doi.org/10.1103/PhysRevLett.95.178102.
Ostoja-Starzewski, M., 2002. Lattice models in micromechanics. Appl. Mech. Rev. 55 (1), 35–60.
Ostoja-Starzewski, M., 2006. Material spatial randomness: From statistical to representative volume element. Probab. Eng. Mech. 21 (2), 112–132.
Ostoja-Starzewski, M., Stahl, D.C., 2000. Random fiber-networks and special elastic orthotropy of paper. J. Elasticity 60, 131–149. https://doi.org/10.1023/A:1010844929730.
Picu, R.C., 2011. Mechanics of random fiber networks—A review. Soft Matter 7 (15), 6768–6785. https://doi.org/10.1039/c1sm05022b.
Romijn, N.E.R., Fleck, N.A., 2007. The fracture toughness of planar lattices: Imperfection sensitivity. J. Mech. Phys. Solids 55 (12), 2538–2564.
Schwaiger, R., Meza, L.R., Li, X., 2019. The extreme mechanics of micro- and nanoarchitected materials. MRS Bull. 44 (10), 758–765.
Shahsavari, A., Picu, R.C., 2012. Model selection for athermal cross-linked fiber networks. Phys. Rev. E 86 (1), 011923. https://doi.org/10.1103/PhysRevE.86.011923.
Shahsavari, A.S., Picu, R.C., 2013. Size effect on mechanical behavior of random fiber networks. Int. J. Solids Struct. 50 (20-21), 3332–3338.
Smith, D.A., Holmberg, V.C., Korgel, B.A., 2010. Flexible germanium nanowires: Ideal strength, room temperature plasticity, and bendable semiconductor fabric. ACS Nano 4 (4), 2356–2362.
Sozumert, E., Farukh, F., Sabuncuoglu, B., Demirci, E., Acar, M., Pourdeyhimi, B., Silberschmidt, V.V., 2020. Deformation and damage of random fibrous networks. Int. J. Solids Struct. 184, 233–247.
Wang, H., Abhilash, A.S., Chen, C., Wells, R., Shenoy, V., 2014. Long-range force transmission in fibrous matrices enabled by tension-driven alignment of fibers. Biophys. J. 107 (11), 2592–2603.
Wu, C., Taghvaee, T., Wei, C., Ghasemi, A., Chen, G., Leventis, N., Gao, W., 2018. Multi-scale progressive failure mechanism and mechanical properties of nanofibrous polyurea aerogels. Soft Matter 14 (38), 7801–7808.
Wu, X.-F., Dzenis, Y.A., 2005. Elasticity of planar fiber networks. J. Appl. Phys. 98 (9), 093501. https://doi.org/10.1063/1.2123369.
Xia, X., Afshar, A., Yang, H., Portela, C.M., Kochmann, D.M., Di Leo, C.V., Greer, J.R., 2019. Electrochemically reconfigurable architected materials. Nature 573 (7773), 205–213.
Yu, Z.-L., Qin, B., Ma, Z.-Y., Huang, J., Li, S.-C., Zhao, H.-Y., Li, H., Zhu, Y.-B., Wu, H.-A., Yu, S.-H., 2019. superelastic hard carbon nanofiber aerogels. Adv. Mater. 31 (23), 1900651. https://doi.org/10.1002/adma.201900651.
Zagar, G., Onck, P.R., Van der Giessen, E., 2011. Elasticity of rigidly cross-linked networks of athermal filaments. Macromolecules 44 (17), 7026–7033.
Zhang, X., Vyatskikh, A., Gao, H., Greer, J.R., Li, X., 2019. Lightweight, flaw-tolerant, and ultrastrong nanoarchitected carbon. Proc. Natl. Acad. Sci. 116 (14), 6665–6672.
Zhu, H., Zhu, S., Jia, Z., Parvinian, S., Li, Y., Vaaland, O., Hu, L., Li, T., 2015. Anomalous scaling law of strength and toughness of cellulose nanopaper. Proc. Natl. Acad. Sci. 112 (29), 8971–8976.